Communication

# Generation of laser-polarized xenon using fiber-coupled laser-diode arrays narrowed with integrated volume holographic gratings

Panayiotis Nikolaou [a,1], Nicholas Whiting [a,1], Neil A. Eschmann [a,2], Kathleen E. Chaffee [a], Boyd M. Goodson [a,*], Michael J. Barlow [b]

[a] Department of Chemistry and Biochemistry, Southern Illinois University, 113 Neckers Hall, Carbondale, IL 62901, USA
[b] Sir Peter Mansfield Magnetic Resonance Centre, University of Nottingham, Nottingham NG7 2RD, UK

ABSTRACT

Volume holographic gratings (VHGs) can be exploited to narrow the spectral output of high-power laser-diode arrays (LDAs) by nearly an order of magnitude, permitting more efficient generation of laser-polarized noble gases for various applications. A $\sim$3-fold improvement in $^{129}$Xe nuclear spin polarization, $P_{Xe}$, (compared to a conventional LDA) was achieved with the VHG-LDA's center wavelength tuned to a wing of the Rb $D_1$ line. Additionally, an anomalous dependence of $P_{Xe}$ on the xenon density within the OP cell is reported—including high $P_{Xe}$ values (>10%) at high xenon partial pressures ($\sim$1000 torr).

© 2008 Elsevier Inc. All rights reserved.

## 1. Introduction

Alkali-metal spin exchange optical pumping (AMSE OP)[3] can generate high nuclear spin polarization in noble gases [1] for a variety of NMR/MRI [2,3] and fundamental physics [4] applications. While different types of light sources have been used to prepare spin-polarized gases via AMSE OP (e.g., Refs. [1–12]), laser-diode arrays (LDAs) have become increasingly dominant because of their high photon flux, low costs, and operational simplicity. However, a key drawback of conventional LDAs is the poor quality of the emitted light—particularly the breadth of their spectral output ($\sim$2–3 nm) compared to atomic lines. The resulting low absorption efficiency can necessitate high incident powers (up to hundreds of Watts), presenting thermal-management problems. Moreover, while this low absorption efficiency can be mitigated by pressure-broadening the alkali spectral line [7,13], this

practice brings on its own complications. To combat these problems, two methods have been developed to constrict the LDA wavelength range: external cavity narrowing [14–16], and more recently—volume holographic grating (VHG) narrowing [17].

Here we report our preliminary investigations of the use of VHG-narrowed LDAs to prepare laser-polarized xenon. Two fiber-coupled LDAs with integrated VHGs provided dramatically narrowed spectral output with high power efficiencies and low costs—allowing more efficient absorption under relatively mild in-cell conditions. Optimal OP (corresponding to a $\sim$3-fold improvement in $^{129}$Xe nuclear spin polarization, $P_{Xe}$) was achieved with the VHG-LDA's center tuned to the wing of the Rb $D_1$ line rather than the center [18,19]. Additionally, changes in the transmitted laser intensity were observed upon magnetic field cycling—enabling an *in situ* estimate of the Rb electronic spin polarization ($P_{Rb}$) [8]. Finally, we report an anomalous dependence of $P_{Xe}$ on the Xe density within the OP cell ([Xe]$_{cell}$)—including unexpectedly high $P_{Xe}$ values (>10%) at high Xe partial pressures ($\sim$1000 torr). These results demonstrate the utility of VHG-narrowed sources for both fundamental AMSE OP studies and hyperpolarized gas applications.

## 2. VHG-LDAs: background and experimental details

External cavity narrowing [14–16] employs planar dispersive gratings to provide feedback to the individual LDA elements; however the optical alignment is critical to maintain feedback to all the elements to ensure acceptable spectral quality and energy effi-

ciency (typically ~40–66% [15,16]), and whether the gratings can withstand sufficiently high intensities is questionable [15]. Alternatively, VHGs (a.k.a. volume Bragg gratings (VBGs)) can achieve LDA spectral narrowing with efficiencies exceeding 90% [20]. VHGs are bulk slabs of photosensitive glass [21] containing Bragg planes of varying index of refraction; in a VHG-based external-cavity diode laser array (VHG-ECDL, Fig. 1(a)) [22], the VHG retro-reflects a narrow band of the laser emission into the LDA elements, forcing them to lase at the injected wavelength. Barlow et al. recently reported a 120 W VHG-ECDL with output near the Rb D$_1$ (794.76 nm) and with a FWHM of 0.24 nm [17].

Details concerning the LDA light sources utilized here are provided immediately below (other experimental aspects are summarized in Section 5). Both VHG-LDAs used in the present work are engineering prototypes from Spectra-Physics/Newport ('**VL1**' is a "Comet" VHG-LDA module, and '**VL2**' is an "Integra" turn-key laser system). **VL1** was mounted to the same TEC / heat sink used by our original 40 W 'standard' LDA (Coherent FAP-B), is driven with the same 65 A diode and TEC-drivers (Newport), and fiber-couples to the same circular-polarizer (CP) optics box (Coherent). **VL1** employs additional slow-axis collimation (SAC) and achromatic lenses after the VHG (thickness: 1.5 mm[21]) to focus the 19 frequency-locked laser elements into a single-core 200 μm silica-clad fiber; **VL1**'s spectral profile is narrowed by nearly an order of magnitude compared to that of our previous LDA (Fig 1(b)), while providing nearly the same power.

**VL2** combines two VHG-LDA modules (each similar to **VL1**) but with simplified optical arrangements: Instead of using FAC or SAC lenses, individual optical fibers (400 μm) are brought within ~600 μm of each laser element (giving 19 fibers/module). The close proximity ensures that each diverging fast-axis beam is launched into its fiber, but requires each module's VHG (placed between the LDA elements and the fibers) to be thin (500 μm)—yielding somewhat reduced spectral narrowing and lineshape quality (Fig. 1(b)). Obtaining the optimal spectral output from **VL2** required overdriving the current (~104%), giving nearly twice the power of **VL1**—albeit with nearly twice the spectral width.

The 1 m optical fibers used with **VL1** and the standard LDA maintain much of their original linear polarization; this 'memory'
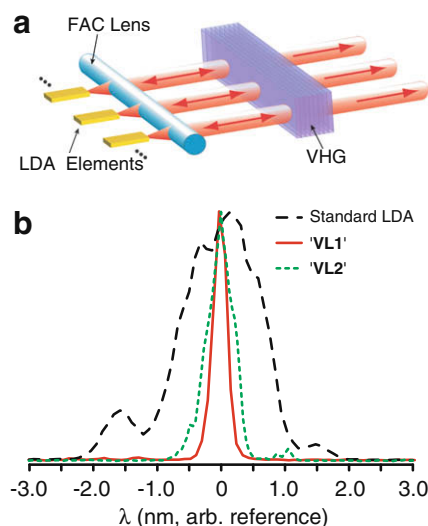
of the LDAs' polarizations affects the power ratio of the two side-by-side circularly-polarized beams emitted from the CP box—causing the ratio of the beam intensities to be sensitive to the strain on the fiber. For the 'standard' LDA, **VL1**, and **VL2**, the nominal beam intensity ratios (straight vs. angled) were ~72:28, ~80:20, and ~55:45, respectively (because of its design, **VL2**'s beam ratio is much closer to unity and less amenable to variation by fiber straining).

Whereas tuning of conventional LDAs may be achieved by varying the LDA temperature (~0.3 nm/°C), the nature of the VHG feedback makes tuning VHG-narrowed LDAs a non-trivial function of LDA temperature and VHG temperature (itself primarily determined by the laser power). A change in the VHG temperature induces a slight change in the element spacing within the VHG, altering the laser's spectral profile. For example, increased driving current for **VL1** (Fig. 2(a)) provides greater laser flux in addition to red-shifting of the centroid towards the Rb D$_1$ center (~0.1 nm/ amp, with operational range of ~0.3 nm); the linewidth also increases. As with **VL1**, the output for **VL2** red-shifts with increased current, but at a reduced rate (~0.006 nm/amp, as a consequence of its design differences); at 94 A (i.e., 47 A/diode, 100% current, 51.6 W at cell) the centroid is ~(−)0.18 nm from the Rb D$_1$ ('blue' side) with a diode temperature of 25 °C, and ~0.09 nm from D$_1$ at
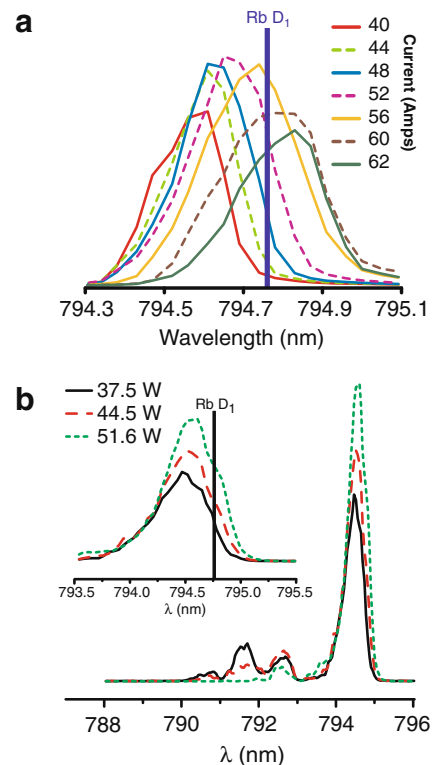
**Fig. 2.** (a) Spectral output of **VL1** as a function of laser diode driving current, showing the lineshape broadening and red-shifting ($\Delta\lambda \sim 0.3$ nm) of the centroid as the laser power increases. FWHM examples: at 40 A: ~0.24 nm; 52 A: ~0.27 nm; 62 A: ~0.33 nm. Position of Rb D$_1$ at 794.76 nm (air referenced) is included for comparison. (b). Spectral output of **VL2** as a function of laser diode driving current (37.5 W: black; 44.5 W: red; 51.6 W: green). Overall lineshape improves with increasing driving current up to its maximum value, and is slightly red-shifted. *Inset:* Close-up view of **VL2** laser output near the Rb D$_1$ line. The less-efficient implementation of the VHG into the design of **VL2** (due in part to the requirement of using thinner VHGs) results in reduced lineshape quality at lower driving currents, particularly regarding the presence of additional features some distance from the main line—indicative of incomplete VHG locking. Such features were not minimized until **VL2** was driven at 104% current (96 A, 54.5 W at cell; not shown). (For interpretation of the references to color in this figure legend, the reader is referred to the web version of this paper.)

**Fig. 1.** (a) Key components of VHG-narrowed LDAs. (b) Normalized output of a standard fiber-coupled LDA (Coherent FAP-B; black, dashed), **VL1** (red, solid), and **VL2** (green, dotted). Conditions: standard LDA: ~32 W (at 47 A), $\Delta\lambda_{FWHM} \approx 2$ nm, $\lambda_{max} \approx 795$ nm; **VL1**: ~26 W (at 50 A), $\Delta\lambda_{FWHM} = 0.27$ nm, $\lambda_{max} = 794.62$ nm; **VL2**: ~55 W (at 96 A), $\Delta\lambda_{FWHM} = 0.49$ nm, $\lambda_{max} = 794.65$ nm. (For interpretation of the references to color in this figure legend, the reader is referred to the web version of this paper.)

35 °C (the nominal **VL2** conditions for OP results presented here). Generally the **VL2** linewidth varies between ∼0.4 and 0.6 nm FWHM.

## 3. Results and discussion

### 3.1. Dependence of $P_{Xe}$, $P_{Rb}$, on VHG-LDA excitation profile

With **VL1**, $P_{Xe}$ is maximized with a driving current of 52 A (Fig. 3(a))—corresponding to an incident power, FWHM, and Rb $D_1$ offset of ∼27 W, ∼0.27 nm, and ∼(−)0.1 nm, respectively. Despite this blue-shifted offset the laser is absorbed quasi-homogeneously by the cell's Rb vapor (i.e., with little distortion of the spectral profile of the transmitted beam besides a small shift; Fig. 3(b))—indicating that the amount of pressure-broadening ($D_1$ FWHM ∼0.1 nm [13]) present under these conditions is already sufficient to achieve efficient absorption of the VHG-narrowed light. When utilizing conventional broadband LDAs, the Rb $D_1$ absorption line is typically 'hole-burned' from the broad and uneven spectral profile—even at the highest described OP cell pressures and temperatures/Rb vapor densities. The optimal **VL1** driving current also provides the highest peak intensity (W vs.



**Fig. 3.** (a) Values of $P_{Xe}$ (blue circles) and $\langle P_{Rb} \rangle$ for the cell's central axis (black squares; estimated via the change in laser transmission during $B_0$ cycling) as functions of **VL1** driver current (and Rb $D_1$ offset), plotted against the laser transmittance at the cell's center (red open circles); the lines are to guide the eye. Approximate $D_1$ offset values are at the top. Conditions: 300 torr Xe, 1700 torr $N_2$, 100 °C, 75 cc cell volume (the gas collision-induced $D_1$ linewidth and shifting should be ∼0.1 nm and ∼(+)0.04 nm, respectively [13]). (b) Near-IR spectra of laser light from **VL1** (mathematically smoothed for clarity) transmitted through the cell near optimal OP conditions (compared with that obtained with a cold cell; black dotted line), showing the effect of magnetic field cycling (with $B_0$ off: red solid line; with $B_0$ on: green dashed line). The integrated differences in the transmitted spectra generated with such field cycling were used to provide the estimates of $\langle P_{Rb} \rangle$ shown in (a). (For interpretation of the references to color in this figure legend, the reader is referred to the web version of this paper.)

FWHM; Fig 2(a)); however, it does not give the highest integrated power or the highest intensity at the Rb $D_1$. Indeed, higher currents yield increased laser flux, as well as red-shifting of the centroid toward the $D_1$ center—but reduced $P_{Xe}$ nearer to true Rb $D_1$ resonance (Fig. 3(a)).

The narrowed lineshape of **VL1** allowed small changes in the amount of laser light transmitted through the cell to be recorded when the external magnetic field ($B_0$) was cycled (Fig. 3(b))—thereby potentially providing an *in situ* measure of $P_{Rb}$. This effect—resulting from Rb $D_1$ 'bleaching' due to depletion pumping of the ground-state magnetic sublevels—has been measured previously using high-resolution lasers [8], but would be difficult to observe with conventional broadband sources. More specifically, this first step of the OP process—whereby the Rb electrons become spin-polarized—leaves a smaller concentration of Rb atoms in the laser-absorbing $m_J$ state (neglecting Rb nuclear spin sublevels). In turn, this population reduction allows slightly more laser light to be transmitted through the cell—allowing $P_{Rb}$ to be estimated from the difference.

Here, the spectral profile of the laser light transmitted through the cell was monitored using a near-IR spectrometer via a pinhole behind the cell.[4] Using a simplistic model (see Appendix) the average Rb polarization along the cell's center axis can be estimated using the relation: $|\langle P_{Rb} \rangle| = (A/A_0) - 1$, where $|\langle P_{Rb} \rangle|$ is the absolute value of the average Rb electron spin polarization along the cell's center, and $A$ and $A_0$ are the laser absorbances when $B_0$ is 'on' and 'off', respectively (Fig. 3(a)). Despite some run-to-run variability, these results may explain the observed Rb $D_1$-offset dependence of $P_{Xe}$: When **VL1** is tuned far from $D_1$ (e.g., with an LDA current of ∼48–50 A), $P_{Xe}$ tracks $\langle P_{Rb} \rangle$ and both are relatively low (while the laser transmittance is high). However when the laser nears resonance (∼58–60 A), $\langle P_{Rb} \rangle$ along the cell's center axis is high, but $P_{Xe}$ is relatively low; here the low laser transmittance at the cell's center directly implies even poorer illumination within a significant portion of the cell's rear and outer regions. Indeed, $P_{Xe}$ is greatest with an intermediate $D_1$ offset where both $\langle P_{Rb} \rangle$ and the transmittance are still relatively high—consistent with optimal $P_{Xe}$ requiring a balance between efficient laser absorption *and* global cell illumination sufficient to minimize xenon depolarization from 'dark' Rb in those regions.

### 3.2. Comparisons of LDA light sources for Xe AMSE OP

Following switching from the standard LDA to **VL1**, we observed a nearly three-fold (W-for-W) improvement in $P_{Xe}$ (Fig. 4).[5] The dependences of $P_{Xe}$ on cell temperature are similar for the two lasers (with and without VHG-narrowing), with **VL1** peaking at a temperature within ∼10 °C of the standard LDA. The relatively mild optimal cell temperature, combined with the $D_1$ offset and the modest fraction of laser light absorbed during optimal conditions, are consistent with the OP being laser-power-limited—despite the high resonant power. Nevertheless, increasing **VL1**'s current to provide greater incident laser flux and improved $D_1$ resonance yielded markedly decreased $P_{Xe}$ values across the entire temperature range (Fig. 4; consistent with the results described in Fig. 3 above).
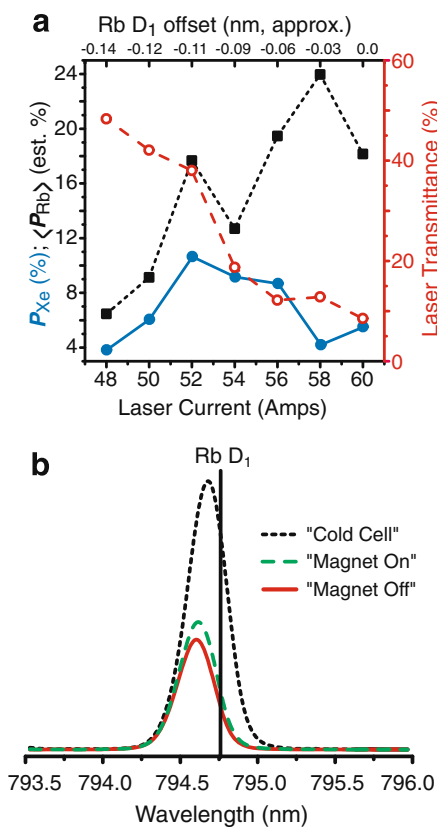
---

[4] Separately, we note it was also possible to utilize the violet (6P→5S) emission from Rb∗–Rb∗ energy-pooling processes (e.g. [23]) as a sensitive *in situ* indicator of laser detuning from the Rb $D_1$ line (when observing the cell under conditions non-optimal for AMSE OP—i.e., low [$N_2$] conditions); somewhat surprisingly, the wavelengths and relative intensities of the Rb lines were more sensitive than expected [13] to buffer gas composition—observations that will be pursued and reported in greater detail elsewhere.

[5] Note that this work describes several sets of experiments that were performed over time under different conditions; correspondingly, while one may draw quantitative comparisons among data sets within the same experiment (e.g. Fig. 4), it is difficult to meaningfully compare absolute $P_{Xe}$ values among different experiments.
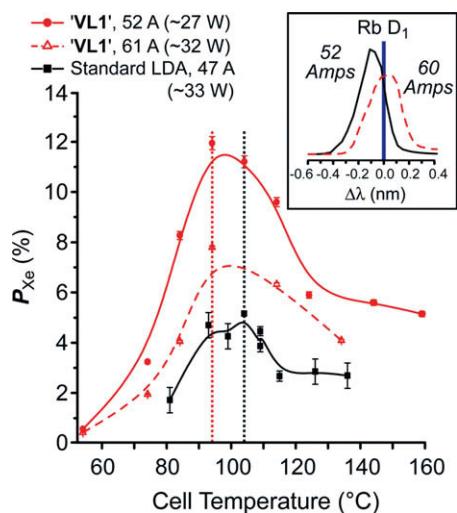
**Fig. 4.** $P_{Xe}$ values obtained with **VL1** (52 A, ~27 W: red circles; 61 A, ~32 W: red open triangles) and a standard LDA (47 A, ~33 W: black squares, from Ref. [23]) as functions of cell surface temperature ([Xe]$_{cell}$ = 300 torr). Optimal temperature appears to be slightly lower for **VL1** (vertical lines). The data's asymmetry about the optimal temperatures is an artifact resulting from higher-temperature OP runs transiting through more-optimal temperatures during cell cool-down [28]. *Inset:* **VL1** output profiles at 52 A (black solid) and 60 A (red dashed), indicating that the improved $P_{Xe}$ observed in the main figure occurs when the laser is tuned slightly from the $D_1$ line. (For interpretation of the references to color in this figure legend, the reader is referred to the web version of this paper.)

The nearly identical Rb $D_1$ offsets for **VL1** and **VL2** under nominal conditions (~0.11 and ~0.09 nm, respectively) enabled their performance for LP Xe generation to be compared. To allow a more direct comparison, the optical fiber for **VL1** was carefully strained until the CP beam ratio was reduced to that of **VL2**. The LP Xe NMR spectra obtained at 9.4 T indicated $P_{Xe}$ enhancement factors of ~8800 ($P_{Xe}$ ~ 7.8%) and ~16,000 ($P_{Xe}$ ~ 14.3%) when using **VL1** vs. **VL2** (respectively). Although **VL1** has a narrower spectral output, this advantage translated into only a small W-for-W $P_{Xe}$ benefit; thus at least under the given conditions, **VL2**'s output was sufficiently narrow to allow its higher total power to be exploited.

In later experiments, further OP optimization with **VL1** as the light source (simultaneous with improved cell preparation) provided routine $P_{Xe}$ values of ~15–17% and ~21–24% (with and without cryo-collection), consistent with ~75% of $P_{Xe}$ surviving the cryo-collection and transfer processes [23].

### 3.3. Dependence of Xe cell density and laser power on OP

Lastly, the minimal change in spectral profile of **VL2** with increasing current was exploited to examine the dependence of $P_{Xe}$ on laser flux at different Xe partial pressures. $P_{Xe}$ would generally be expected [8,9,24,25] to decrease smoothly and dramatically with increasing Xe density; the xenon polarization becomes 'capped' by corresponding reductions in the values of $P_{Rb}$ that can be achieved (given the strong contribution to the Rb spin-destruction rate from increased Rb/Xe collisions [1,26]). Thus, most AMSE OP setups typically employ relatively low running Xe partial pressures (~1–70 torr) to achieve high (>10%) $P_{Xe}$ values—potentially limiting some applications that simultaneously require both high Xe densities/amounts *and* high $P_{Xe}$.

Instead, we have reproducibly observed a different trend (Fig. 5) wherein $P_{Xe}$ initially rises with increasing [Xe]$_{cell}$, peaks, and then falls off but remains relatively high (>10%)—even at ~1000 torr Xe—to give among the highest $P_{Xe}$ yet reported at such high [Xe]$_{cell}$ values. We note that a similar qualitative trend was also observed in an initial study using **VL1** [19] and the effect does not appear to
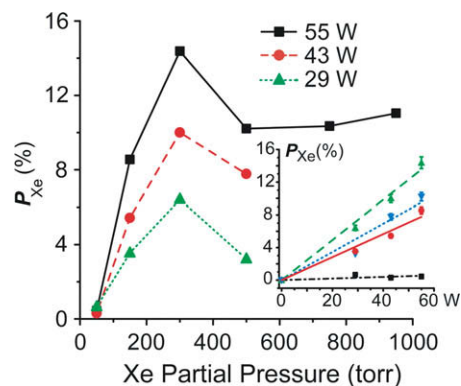


**Fig. 5.** $P_{Xe}$ vs. [Xe]$_{cell}$ (with variable Xe partial pressure, but constant cell pressure of 2000 torr, backfilled with $N_2$) at various **VL2** laser powers (55 W: black squares; 43 W: red circles; 29 W: green triangles). *Inset:* Same data, but with $P_{Xe}$ plotted as a function of laser power for different Xe loadings; data points are fitted to lines (forced through zero). 50 torr: black squares (dotted-dashed); 150 torr: red circles (solid); 300 torr: green triangles (dashed); 500 torr: blue inverted triangles (dotted). (For interpretation of the references to color in this figure legend, the reader is referred to the web version of this paper.)

be an artifact of cell contamination or variances in Xe collection efficiency. Moreover, laser energy-dependent mechanisms (e.g., involving highly elevated internal temperatures of the $N_2$ buffer gas [27]) may affect the OP process, but do not appear to cause the observed dependence of [Xe]$_{cell}$ on $P_{Xe}$ given that similar trend lines are observed at various incident laser powers (Fig. 5). Indeed, the data shows the potential utility of additional laser flux, as $P_{Xe}$ rises almost linearly with power (except at low [Xe]$_{cell}$—Fig. 5 *inset*). While the origin of the anomalous dependence of $P_{Xe}$ on [Xe]$_{cell}$ is not yet understood, ongoing studies with *in situ* low-field NMR polarimetry [28] indicate that the effect involves an interplay between [Xe]$_{cell}$ and the overall cell temperature—suggesting a route to further $P_{Xe}$ improvements as these effects are explored in greater detail.

### 4. Conclusions

We have shown that the LDA line-narrowing endowed by VHGs can improve spin-polarized gas production under relatively mild conditions—demonstrating the utility of VHG-LDAs for fundamental AMSE OP studies, as well as for a variety of NMR/MRI applications. While altering the spectral profiles of the VHG-LDAs utilized here generally requires varying the output power, next-generation VHG-LDAs capable of providing true tunability at the Rb $D_1$ wavelength should become available in the near future [29,30]—a desirable capability in light of the observed dependence of $P_{Xe}$ on the $D_1$ offset. Finally, while the present data were derived from 'batch-mode' Rb/$^{129}$Xe OP, we expect that the demonstrated advantages will translate well to OP setups employing alternate configurations [7,11,12,31–34], alkali metals [1,35], and/or noble gas isotopes [1,36,37].

### 5. Experimental

The non-LDA components of the Xe OP apparatus have been described previously [23]. Briefly, the OP apparatus—centered around a Rosen[9] cell (75 cc inner cell volume) residing in a Helmholtz coil (HC) pair (22″ i.d., ~30 G, Walker Magnetics)—permits operation in either batch or "stop-flow" mode and allows for arbitrary gas mixtures of Xe, $N_2$, and He. Nominal OP conditions: single-batch-mode OP; binary Xe/$N_2$ gas mixture; cell gas pressures: 300 torr Xe, backfilled with $N_2$ gas to give ~2000 torr total pressure; and 15 min. OP time. Following OP, the Xe may be efficiently collected by using a spiral glass liquid-$N_2$-cooled condenser resid-

ing in a strong ($\sim$1500 G) field provided by two permanent magnets (Indigo Inst.); alternatively, the contents of the cell can be simply expanded into an evacuated volume including the NMR tube. Optical emission from the lasers and/or excited Rb vapor was monitored via fiber optic probes connected to UV/visible and near-IR portable spectrometers (Ocean Optics USB2000 and HR2000+, respectively). High-field $^{129}$Xe NMR spectra were recorded at 9.4 T (110.6 MHz) using a Varian Inova spectrometer. Laser-polarized (LP) Xe spectra were obtained with a single 1 μs rf pulse ($\alpha$ = 6.7°); corresponding thermally polarized Xe signals were obtained from the same sample following careful addition of sufficient $O_2$ gas to reduce the $^{129}$Xe $T_1$ (to a few s) to permit signal averaging ($\alpha$ = 90°; typical recycle delay = 20 s).

## Note Added in Proof

Very recently, continued optimization of our OP setup with **VL1** (aided by low-field nuclear polarimetry and exploitation of the apparent dependence of the optimal cell temperature upon [Xe] cell) has yielded further improvements in the xenon nuclear spin polarization at high xenon densities (including PXe values of $\sim$55%, $\sim$32%, $\sim$23%, and $\sim$11% at 50, 300, 500, and 2000 torr Xe, respectively); these results will be investigated and presented in greater detail elsewhere.

## Acknowledgments

## Appendix A

Changes in the spectral profiles of the transmitted laser light caused by cycling $B_0$ can be integrated to estimate the average Rb polarization along the central axis of the cell ($\langle P_{Rb} \rangle$) using a simplistic model. While the measurement of $P_{Rb}$ via optical transmission methods has been the subject of considerable previous work (e.g., Refs. [38–40]), the experimental conditions for the present work were sufficiently different to warrant an alternate approach (and corresponding set of assumptions). Here we assume: a near absence of any significant population of electronically excited Rb* [1]; $\approx$100% circularly-polarized light; a constant total Rb number density across the cell ($N_T$); and $P_{Rb} \approx 0$ when $B_0 = 0$.

Adapted from Beer's Law,

$$A = -\ln T = -\ln\left(\frac{I_{hot}}{I_{cold}}\right), \tag{A1}$$

where $A$ is the absorbance, $T$ is the transmittance, and here $I_{hot}$ and $I_{cold}$ are determined by integrating the intensities of the transmitted laser spectra obtained when a gas-loaded cell is, respectively, 'hot' and 'cold' (i.e., with and without Rb vapor present). Since only those Rb atoms in one of the two ground-state magnetic sublevels can act as absorbers (say $m_J$ = +1/2 with $\sigma^-$ light), $A$ is given by:

$$A = \sigma(\lambda)l\langle N^+ \rangle, \tag{A2}$$

where $\sigma(\lambda)$ is the (wavelength-dependent) absorption cross-section for the Rb vapor, $l$ is the path length, and $\langle N^+ \rangle$ is the number density

of Rb atoms in the $m_J$ = +1/2 spin state (averaged along the long axis of the cell). Next,

$$\langle P_{Rb} \rangle = \frac{\langle N^+ \rangle - \langle N^- \rangle}{N_T}, \tag{A3}$$

where $N_T = \langle N^+ \rangle + \langle N^- \rangle$. Since $\langle P_{Rb} \rangle \approx 0$ when $B_0 = 0$, $\langle N^+ \rangle$ under these conditions is given by: $\langle N_0^+ \rangle 0.5 * N_T$. The terms $\sigma(\lambda)$ and $l$ cancel when $A$ is divided by $A_0$ (the absorbance when $B_0 = 0$) to give ($A/A_0$) = $2\langle N^+ \rangle/N_T$. Rearranging Eq. (A3) and combining with the relationship for ($A/A_0$) gives:

$$|\langle P_{Rb} \rangle| = \frac{A}{A_0} - 1, \tag{A4}$$

where the absolute value is taken because the differential absorbance will be insensitive to the light helicity.

Because the Rb polarization at each position within the cell will rapidly reach steady state with the resonant laser flux (and because the illumination decreases not only along $z$ (the long axis of the cell) but radially outward from this central axis as well), the Rb polarization will generally be a function of both $z$ and $r$ ($P_{Rb}(z,r)$). Thus since in our experiments the transmitted light is sampled via a pinhole in the beam-stop behind the cell, the value of $P_{Rb}$ that is provided is really a $z$-averaged measurement of $P_{Rb}$ for $r \approx 0$, and this $\langle P_{Rb} \rangle$ value can be expected to overestimate the cell-averaged value of $P_{Rb}$—particularly under conditions of highly non-uniform illumination (e.g., under high-absorbance conditions). Separately, this approach would *under*estimate $P_{Rb}$ if a sufficiently-strong residual magnetic field persisted when $B_0$ is turned off.

## References

[1] T. Walker, W. Happer, Spin-exchange optical pumping of noble-gas nuclei, Rev. Mod. Phys. 69 (1997) 629–642.
[2] B.M. Goodson, Nuclear magnetic resonance of laser-polarized noble gases in molecules, materials, and organisms, J. Magn. Reson. 155 (2002) 157–216.
[3] A. Bifone, A. Cherubini, Hyperpolarised Xenon in Biology, Prog. Nucl. Magn. Reson. Spectrosc. 42 (2003) 1–30.
[4] J.L. Friar, B.F. Gibson, G.L. Payne, A.M. Bernstein, T.E. Chupp, Neutron polarization in polarized 3He targets, Phys. Rev. C 42 (1990) 2310–2314.
[5] M.E. Wagshul, T.E. Chupp, Optical pumping of high-density Rb with a broadband dye laser and GaAlAs diode laser arrays: application to 3He polarization, Phys. Rev. A 40 (1989) 4447–4454.
[6] M.P. Augustine, K.W. Zilm, Optical pumping magnetic resonance in high magnetic fields: characterization of nuclear relaxation during pumping, J. Chem. Phys. 105 (1996) 2998–3011.
[7] B. Driehuys, G.D. Cates, E. Miron, K. Sauer, D.K. Walter, W. Happer, High-volume production of laser-polarized Xe-129, Appl. Phys. Lett. 69 (1996) 1668–1670.
[8] U. Ruth, T. Hof, J. Schmidt, D. Fick, H.J. Jansch, Production of nitrogen-free, hyperpolarized 129Xe gas, Appl. Phys. B 68 (1999) 93.
[9] M.S. Rosen, T.E. Chupp, K.P. Coulter, R.C. Welsh, S.D. Swanson, Polarized 129Xe optical pumping/spin exchange and delivery system for magnetic resonance spectroscopy and imaging studies, Rev. Sci. Instrum. 70 (1999) 1546–1552.
[10] H. Desvaux, T. Gautier, G. Le Goff, M. Petro, P. Berthault, Direct evidence of a magnetization transfer between laser-polarized xenon and protons of a cage-molecule in water, Eur. Phys. J. 12 (2000) 289–296.
[11] A.L. Zook, B.B. Adhyaru, C.R. Bowers, High capacity production of >65% spin polarized xenon-129 for NMR spectroscopy and imaging, J. Magn. Reson. 159 (2002) 175–182.
[12] I.C. Ruset, S. Ketel, F.W. Hersman, Optical pumping system design for large production of hyperpolarized 129Xe, Phys. Rev. Lett. 96 (2006) 053002.
[13] M.V. Romalis, E. Miron, G.D. Cates, Pressure broadening of Rb D-1 and D-2 lines by He-3, He-4, N-2 and Xe: line cores and near wings, Phys. Rev. A 56 (1997) 4569–4578.
[14] I.A. Nelson, B. Chann, T.G. Walker, Spin-exchange optical pumping using a frequency-narrowed high power diode laser, Appl. Phys. Lett. 76 (2000) 1356.
[15] H. Zhu, I.C. Ruset, F.W. Hersman, Spectrally narrowed external-cavity high-power stack of laser diode arrays, Opt. Lett. 30 (2005) 1342–1344.
[16] E. Babcock, B. Chann, I.A. Nelson, T. Walker, Frequency-narrowed diode array bar, Appl. Opt. 44 (2005) 3098–3104.
[17] M.J. Barlow, 47th Exptl. Nucl. Magn. Reson. Conf, Pacific Grove, CA, 2006.
[18] R.W. Mair, M.J. Barlow, M.S. Rosen, R.L. Walsworth, Improved noble gas polarization production for porous and granular media studies using narrowed-line VBG laser sources, Magn. Reson. Imaging 25 (2007) 549.
[19] P. Nikolaou, N. Whiting, K.E. Chaffee, I. Saha, M.J. Barlow, B.M. Goodson, 48th Exptl. Nucl. Magn. Reson. Conf., Daytona, FL, 2007.

[20] A. Gourevitch, G. Venus, V. Smirnov, D.A. Hostutler, L. Glebov, Continuous wave, 30 W laser-diode bar with 10 GHz linewidth for Rb laser pumping, Opt. Lett. 33 (2008) 702–704.

[21] C. Moser, G. Steckman, Photonics Spectra (2005) 82.

[22] B.L. Volodin, S.V. Dolgy, E.D. Melnik, E. Downs, J. Shaw, V.S. Ban, Wavelength stabilization and spectrum narrowing of high-power multimode laser diodes and arrays by use of volume Bragg gratings, Opt. Lett. 29 (2004) 1891–1893.

[23] I. Saha, P. Nikolaou, N. Whiting, B.M. Goodson, Characterization of violet emission from Rb optical pumping cells used in laser-polarized xenon NMR experiments, Chem. Phys. Lett. 428 (2006) 268–276.

[24] M.G. Mortuza, S. Anala, G.E. Pavlovskaya, T.J. Dieken, T. Meersmann, Spin-exchange optical pumping of high-density xenon-129, J. Chem. Phys. 118 (2003) 1581–1584.

[25] A. Fink, D. Baumer, E. Brunner, Production of hyperpolarized xenon in a static pump cell: Numerical simulations and experiments, Phys. Rev. A 72 (2005) 053411.

[26] G.D. Cates, R.J. Fitzgerald, A.S. Barton, P. Bogorad, M. Gatzke, N.R. Newbury, B. Saam, Rb-129Xe spin-exchange rates due to binary and three-body collisions at high Xe pressures, Phys. Rev. A 45 (1992) 4631–4639.

[27] D.K. Walter, W.M. Griffith, W. Happer, Energy transport in high-density spin-exchange optical pumping cells, Phys. Rev. Lett. 86 (2001) 3264–3267.

[28] N. Whiting, P. Nikolaou, N. Eschmann, M.J. Barlow, B.M. Goodson, 49th Exp. Nucl. Magn. Reson. Conf., Asilomar, CA, 2008.

[29] M.J. Barlow, C.-H. Li, R.W. Mair, M.S. Rosen, R.L. Walsworth, N. Whiting, P. Nikolaou, K.E. Chaffee, I. Saha, B.M. Goodson, K.F. Stupic, Z.I. Cleveland, G.E. Pavlovskaya, T. Meersmann, 48th Exp. Nucl. Magn. Reson. Conf., Daytona, FL, 2007.

[30] A.B. Petersen, J. Gloyd, Tunable, high power, narrow band emission from a volume grating-controlled diode bar, Adv. Solid-State Photonics, 2008.

[31] K. Knagge, J. Prange, D. Raftery, A continuously recirculating optical pumping apparatus for high xenon polarization and surface NMR studies, Chem. Phys. Lett. 397 (2004) 11–16.

[32] N.J. Shah, T. Unlu, H.-P. Wegener, H. Halling, K. Zilles, S. Appelt, Measurement of rubidium and xenon absolute polarization at high temperatures a a means of improved production of hyperpolarized 129Xe, NMR Biomed. 13 (2000) 214–219.

[33] T. Su, G.L. Samuelson, S.W. Morgan, G. Laicher, B. Saam, Liquid hyperpolarized Xe-129 produced by phase exchange in a convection cell, Appl. Phys. Lett. 85 (2004) 2429–2431.

[34] A. Fink, E. Brunner, Optimization of continuous flow pump cells used for the production of hyperpolarized 129Xe: a theoretical study, Appl. Phys. B 89 (2007) 65–71.

[35] E. Babcock, I. Nelson, S. Kadlecek, B. Driehuys, L.W. Anderson, F.W. Hersman, T.G. Walker, Hybrid spin-exchange optical pumping of 3He, Phys. Rev. Lett. 91 (2003) 123003.

[36] J.C. Leawoods, D.A. Yablonskiy, B. Saam, D.S. Gierada, M.S. Conradi, Hyperpolarized He-3 gas production and MR imaging of the lung, Concepts Magn. Reson. 13 (2001) 277–293.

[37] Z.I. Cleveland, G.E. Pavlovskaya, K.F. Stupic, C.F. LeNoir, T. Meersmann, Exploring hyperpolarized 83Kr by remotely detected NMR relaxometry, J. Chem. Phys. 124 (2006) 044312.

[38] H. Gibbs, Importance of nuclear-spin effects in extracting alkali spin-exchange cross sections from zeeman optical-pumping signals, Phys. Rev. 139 (1965) 1374–1391.

[39] H.M. Gibbs, R.J. Hull, Spin-exchange cross sections for Rb87–Rb87 and Rb87–Cs133 collisions, Phys. Rev. 153 (1967) 132–151.

[40] D. Tupa, L.W. Anderson, Effect of radiation trapping on the polarization of an optically pumped alkali-metal vapor, Phys. Rev. A 33 (1986) 1045–1051.